Enhanced tumor targeting and penetration of fluorophores via iRGD peptide conjugation: a strategy for the precision targeting of lung cancer

Yunlong Li[1], Chenmei Li[1], Jiamin Li[2], Dong Han[1], Gang Xu[3], Daolong Zhu[3], Huiming Cai[4], Yiqing Wang[1], Dong Wang[3]

[1]Department of Biomedical Engineering, College of Engineering and Applied Sciences, State Key Laboratory of Analytical Chemistry for Life Science, Nanjing University, Nanjing, China; [2]College of Life Sciences, Anhui Agricultural University, Hefei, China; [3]Department of Thoracic Surgery, Taikang Xianlin Drum Tower Hospital, Affiliated Hospital of Medical School, Nanjing University, Nanjing, China; [4]Nanjing Nuoyuan Medical Devices Co., Ltd., Nanjing, China

Contributions: (I) Conception and design: Y Wang; (II) Administrative support: H Cai, Y Wang; (III) Provision of study materials or patients: Y Li, D Zhu; (IV) Collection and assembly of data: Y Li, J Li, G Xu; (V) Data analysis and interpretation: Y Li; (VI) Manuscript writing: All authors; (VII) Final approval of manuscript: All authors.

Correspondence to: Yiqing Wang, PhD. Department of Biomedical Engineering, College of Engineering and Applied Sciences, State Key Laboratory of Analytical Chemistry for Life Science, Nanjing University, Qixia District, Xianlin Road No. 163, Nanjing 210023, China. Email: wangyiqing@nju.edu.cn; Huiming Cai, MS. Nanjing Nuoyuan Medical Devices Co. Ltd., Qinhuai District, Ziyun Road No. 18, Nanjing 211514, China. Email: chm9166@aliyun.com; Dong Wang, PhD. Department of Thoracic Surgery, Taikang Xianlin Drum Tower Hospital, Affiliated Hospital of Medical School, Nanjing University, Qixia District, Lingshan North Road No. 188, Nanjing 210046, China. Email: wangdong_nj001@126.com.

Background: Accurate real-time tumor delineation is essential for achieving curative resection (R0 resection) during non-small cell lung cancer (NSCLC) surgery. The unique characteristics of lung tissue structure significantly challenge the use of video-assisted thoracoscopic surgery in the identification of lung nodules. This difficulty often results in an inability to discern the margins of lung nodules, necessitating either an expansion of the resection scope, or a transition to open surgery. Due to its high spatial resolution, ease of operation, and capacity for real-time observation, near-infrared fluorescence (NIRF) navigation in oncological surgery has emerged as a focal point of clinical research. Targeted NIRF probes, which accumulate preferentially in tumor tissues and are rapidly cleared from normal tissues, enhance diagnostic sensitivity and surgical outcomes. The imaging effect of the clinically approved NIRF probe indocyanine green (ICG) varies significantly from person to person. Therefore, we hope to develop a new generation of targeted NIRF probes targeting lung tumor-specific targets.

Methods: First, the peptide iRGD (sequence: CRGDKGPDC) fluorescent tracer was synthesized, and characterized through mass spectrometry (MS), proton nuclear magnetic resonance (^{1}H NMR), and high-performance liquid chromatography (HPLC). Fluorescence properties were tested subsequently. Safety was performed *in vitro* using both human normal liver cells and human normal breast cells. Second, Metabolism and optimal imaging time were determined by tail vein injection of iRGD fluorescent tracer. Finally, Orthotopic and metastatic lung tumor models were used to evaluate the targeting properties of the iRGD fluorescent tracer.

Results: We successfully synthesized an iRGD fluorescent tracer specifically designed to target NSCLC. The molecular docking analyses indicated that this tracer has receptor affinity comparable to that of iRGD for αvβ3 integrin, with a purity ≥98%. Additionally, the tracer is highly soluble in water, and its excitation and emission wavelengths are 767 and 799 nm, respectively, positioning it within the near-infrared spectrum. The cellular assays confirmed the tracer's minimal cytotoxicity, underscoring its excellent biosafety profile. *In vivo* studies further validated the tracer's capacity for specific NSCLC detection at the cellular level, alongside a prolonged imaging window of 6 days or more. Notably, the tracer demonstrated superior specificity in localizing very small lung nodules, which are otherwise clinically indiscernible, outperforming

non-targeted ICG. Fluorescence intensity analyses across various organs revealed that the tracer is predominantly metabolized by the liver and kidneys, with excretion via bile and urine, and exhibits minimal toxicity to these organs as well as the lungs.

Conclusions: The iRGD fluorescent tracer selectively accumulates in NSCLC tissues by specifically targeting αvβ3 receptors, which are overexpressed on the surface of tumor cells. This targeted approach facilitates the real-time intraoperative localization of NSCLC, presenting an improved strategy for intraoperative tumor identification with significant potential for clinical application.

Keywords: Pulmonary nodule; iRGD; tumor-targeted; near-infrared fluorescence surgery (NIRF surgery); αvβ3

Introduction

According to the latest statistics from the World Health Organization, lung cancer continues to be the primary cause of cancer-related fatalities, and accounted for approximately 1.8 million deaths in 2020 (1). Surgery is the preferred treatment modality for lung cancer. Currently, the more commonly used surgical procedures for early stage lung cancer in the clinic are lung wedge resection and segmental resection (2,3). Clinical data have shown that the precise resection of cancer significantly prolongs the five-year survival of patients (4,5).

Highlight box

Key findings

- Targeting-integrin αvβ3 imaging is an innovative targeting approach. iRGD-ZW800 can specifically recognize αvβ3 and transport the tracer into the tumor, enabling the stable and precise intraoperative localization of lung nodules guided by fluorescence imaging.

What is known and what is new?

- cRGD-ZW800-1 is the first zwitterionic integrin-targeted fluorescent agent translated to the clinic. It enables colon cancer visualization during minimally invasive laparoscopic surgery.
- iRGDZW800 has been proven to specifically target αvβ3-overexpressed tumors and was applied to the localization of lung cancer.

What is the implication, and what should change now?

- This new type of targeted near-infrared tracer can assist doctors in performing rapid and precise lung nodule resection under fluorescence guidance. In the future, iRGD-ZW800 could be used as an alternative for the real-time positioning of pulmonary nodules during surgery.

Current tumor diagnostic methods, including magnetic resonance imaging and computed tomography (CT), face challenges in achieving the real-time intraoperative determination of the benign or malignant status of lung cancer margins. These difficulties stem from the cumbersome nature of the equipment, complex operation procedures, and time-intensive analysis of data (6-9). In recent years, near-infrared fluorescence (NIRF) navigation in tumor surgery has increasingly become a focal point of clinical science and applied research. This interest is attributed to its high spatial resolution, ease of operation, and capability for real-time observation.

Indocyanine green (ICG) is currently the primary tracer used in 75% of NIRF navigational procedures worldwide (10). ICG faces limitations such as the optimal injection dose and imaging time varying from person to person, lack of tumor specificity, and poor fluorescence stability. It is unable to accurately locate cancer during surgery and provide doctors with real-time tumor localization information (11). As a result, the pharmacokinetics of ICG are strongly influenced by differences in tissue microstructure, as well as other patient markers [e.g., liver function (12)], leading to large individual differences in tumor imaging effects. ICG does not have the ability to target cancer cells. Suboptimal sensitivity or false positives have been widely reported in various lung cancer clinical trials. Clearly, specific tumor-targeting probes are needed to help surgeons identify and treat lung cancer.

The expression of integrin αvβ3 is significantly increased in the blood vessels and on the cell surfaces of various tumors, marking it as a crucial element of the tumor microenvironment (13). Numerous studies have confirmed that integrin αvβ3 is overexpressed on the surface of

neovascular endothelial cells and in malignant gliomas, breast cancer, gastric cancer, lung cancer, and melanoma (14-17). Consequently, integrin αvβ3 has emerged as an ideal candidate for tumor imaging and therapeutic applications. To date, a limited number of αvβ3-targeted fluorescent probes, such as cRGD-ZW800-1 (18), RGD-nanoparticles (19), and IRDye 800CW RGD (20), have been developed and are undergoing clinical evaluation. However, the use of cRGD as a targeting agent frequently encounters challenges related to tumor penetration depth. iRGD, a novel small molecule peptide explored in recent research, has the capability to actively bind to cell surface receptors and penetrate both the intercellular matrix and cell membranes, thereby facilitating the transport of substances into cells (21,22). In this study, we harnessed the iRGD peptide in conjunction with an NIRF tracer, enhancing the molecular probe's ability to actively target tumor cells, and leveraging iRGD cell penetration properties to convey the tracer into deeper tumor regions. This approach enabled the precise localization of both *in situ* lung tumors and metastases. We present this article in accordance with the ARRIVE reporting checklist (available at https://tlcr.amegroups.com/article/view/10.21037/tlcr-24-589/rc).

Methods

Reagents and instruments

Chemical reagents

The ICG used in this experiment was produced by Dandong Yichuang Pharmaceutical Co., Ltd. (Dandong, China). All the other chemicals of analytical grade were acquired from Aladdin reagent.

Biological reagents

Dulbecco's Modified Eagle Medium, Roswell Park Memorial Institute Medium 1640, fetal bovine serum, penicillin/streptomycin trypsin-EDTA (0.25%), phosphate buffered saline (PBS), 4% paraformaldehyde, and the A549, LLC1, and 4T1 cell lines were purchased from Jiangsu KeyGEN BioTECH Co., Ltd. (Nanjing, China).

Instruments

The IVIS Spectral Imaging System was purchased from PerkinElmer (Waltham, MA, USA) and used for fluorescence imaging. Nanjing Nuoyuan Medical Co., Ltd. (Nanjing, China) provided Real-IGS FLI-10B for intraoperative imaging. The UV-Vis absorption spectrum was acquired by UV-2500 from Shimadzu (Kyoto, Japan). The fluorescence emission spectrum was acquired by RF-6000 from Shimadzu (Kyoto, Japan). Analytical high-performance liquid chromatography (HPLC) was performed with an Agilent 1100 System (Shimadzu, Kyoto, Japan). Liquid chromatography-mass spectrometry (LC-MS) was performed using the RapidFire 400 System (Shimadzu, Kyoto, Japan).

Animals

A total of 17 (4-week-old) healthy Balb/c nude mice, 3 (4-week-old) BALB/c mice, and 3 (4-week-old) C57BL/6 mice were obtained from GemPharmatech Co., Ltd. (Nanjing, China) (Animal License No. SYXK [Su] 2019-0056). Animal experiments were performed under a project license (No. IACUC-2403007) granted by ethics committee of Nanjing University, in compliance with Chinese national guidelines for the care and use of animals. The mice were kept in a specific-pathogen-free environment and given free access to sterile water and food.

Synthesis of iRGD-ZW800

The ZW800-1 and iRGD-ZW800 heptamethine cyanine fluorophores were prepared as described previously (23). iRGD (MW 948.04) was synthesized by standard Fmoc-based solid phase peptide chemistry. First, the protected linear peptide Cys(Acm)-Arg(Pbf)-Gly-Asp(OBut)-Lys(Boc)-Gly-Pro-Asp(OBut)-Cys(Acm) was assembled on Rink amide resin. Disulfide bonds were formed on the solid support in a DMF solution containing thallium trifluoroacetate. ZW800-1 was conjugated to the N-terminus of the iRGD peptide by Fmoc chemistry. The product was deprotected in a phenyl sulfide solution containing trifluoroacetic acid and triisopropylsilane to get iRGD-ZW800.

Molecular docking

The protein structure with PDB-ID 1L5G was obtained from the RCSB Protein Data Bank. First: prepare the protein structure in Chimera. This protein structure was prepared by removing the ligand and running Dock Prep to minimize the structure. Then the dye conjugate was drawn in ChemDraw, protonation and UFF minimization were done with the RD kit. Charges were calculated by mmff94.

Finally: docking was done using SMINA with a seed of 0, centered on the original ligand, autobox add parameter of 15, and exhaustiveness parameter of 24.

Assessment of cell toxicity

About 10^4 L02 and HEK-293 cells were added to 96-well plates in a volume of 90 µL. Different doses of iRGD-ZW800 in the culture medium were configured into a concentration gradient of 1 mM, 100 µM, 10 µM, 1 µM, 100 nM, 10 nM, 1 nM, and 0.1 nM. The cells were cultured in an incubator for 24 h at 37 ℃ and 5% carbon dioxide. Subsequently, the MTT method was used to detect cell viability. The method was as follows: MTT was prepared into a 5 mg/mL pbs solution, and 10 µL MTT solution was added to each well. After 2 h of culture, 200 µL dimethyl sulfoxide (DMSO) was added to each well to dissolve the formazan crystals. The absorption intensity was detected using a microplate reader. The test wavelength was 570 nm and the reference wavelength was 630 nm. The IC_{50} value was calculated using Graphpad10.1.2.

Establishment and imaging of three different animal models

Establishment and imaging of a non-small cell lung cancer (NSCLC) subcutaneous tumor mouse model

The BALB/c nude mice were anesthetized with isoflurane, and 10^7 A549 cells were injected subcutaneously into the left armpit in 100 µL of PBS. Tumor size was measured on the 3rd day after tumor formation. The long and short diameters of the tumors were measured with vernier calipers, and the tumor size was calculated using the following formula: $V=a^2b\pi/2$, where "a" is the short diameter of the tumor, and "b" is the long diameter of the tumor. When the tumor grew to 100 mm^3, the IVIS imaging system was used to detect the fluorescence intensity of the tumor and normal tissues at different time points. Next, 10 nmol of animal iRGD-ZW800 tracer was injected into the tail vein of the three animals, and imaged at 1 h, 2 h, 4 h, 8 h, 12 h, 24 h, 2 d, 3 d, 4 d, and 5 d respectively, and the fluorescence intensity at different time points was detected. The tumor-to-background ratio was calculated. In addition, 10 nmol of animal iRGD-ZW800-1 tracer was injected into the tail vein of the animals. The animals were sacrificed 24 h later, and their organs were taken out to detect fluorescence intensity.

Establishment and imaging of an orthotopic lung cancer model in C57BL/6 mice

After the mice were anesthetized, they were fixed on the operating table in a supine position. The anterior chest wall of each mouse was disinfected with alcohol. A small incision of about 5 mm was made at the costal arch of the left anterior axillary line. The skin and subcutaneous tissue were separated and exposed to the chest wall. Cell suspension (50 µL) and Matrigel (50 µL) were mixed. Before rapid coagulation, 100 µL of LLC1 cells and Matrigel suspension were injected into the left lung of the mouse with an insulin injection needle. The needle was inserted about 3 mm. After the injection, the needle was stopped for 5 s, and the needle was then withdrawn. The incision was then sutured. Three weeks later, 10 nmol of iRGD-ZW800 was injected into the tail vein, and 24 h later, the mouse were thoraxed and imaged using FLI-10B. The control group mice were injected with 100 nmol of ICG. After 24 h, the chest of each mouse was opened, and the lungs were imaged using FLI-10B. In order to evaluate the imaging effect of iRGD-ZW800 tracer on tumor boundary, a straight line was drawn between normal lung and tumor, and the decreasing rate of fluorescence intensity on the straight line was measured. The faster the fluorescence intensity decreased between lung and tumor, the more obvious the tumor boundary was.

Establishment and imaging of a mouse model with the lung metastasis of 4T1 breast cancer cells

Establishment and imaging of an experimental lung metastasis model

First, the cell suspension was prepared. Each Balb/c mouse was injected with 10^7 4T1 cells through the tail vein. The living conditions of the mice were observed every week. After four weeks, 10 nmol of iRGD-ZW800 was injected into the tail vein, and 4 h later, the chest was opened, and the lungs were imaged using FLI-10B. The control group mice were injected with 100 nmol of ICG. After 24 h, the chest of each mouse was opened, and the lungs were imaged using FLI-10B.

Establishment and imaging of spontaneous lung metastasis model

The 4T1 cells were digested with trypsin, centrifuged at 1,000 r/min for 5 min, and resuspended in PBS to prepare the cell suspension. Each Balb/C nude mouse was inoculated subcutaneously with 10^7 4T1/mouse in PBS in the neck. The tumor formation in the nude mice was observed every 2 days, and the long and short diameters of
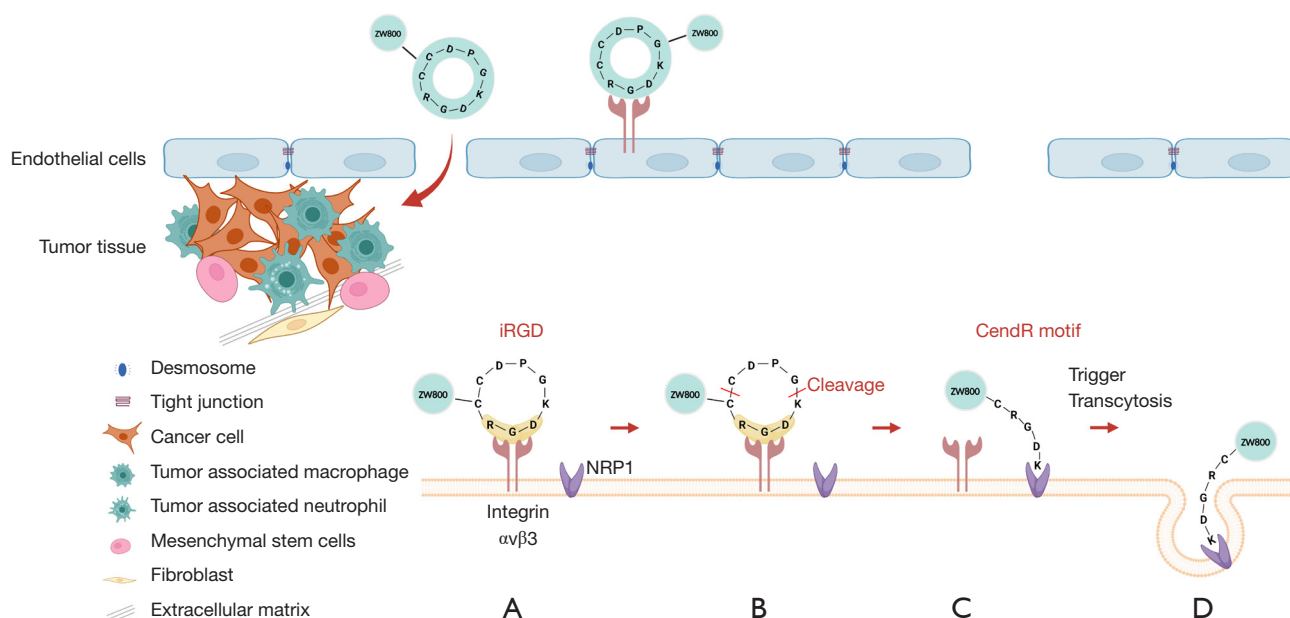
Figure 1 Schematic representation of iRGD-activated tumor targeting for tracer solid tumor delivery. (A) First, the iRGD (CRGD[K/R]GP[D/E]C) peptide binds to the αvβ3 integrin in tumorigenic endothelial cells. (B) iRGD is proteolytically cleaved to produce CRGD/K and expose the CendR motif at the C-terminus. (C) Next, CendR binds to NRP-1 in the tumor tissue. (D) Finally, internalization into the tumor sites via endocytosis is achieved. This image is adapted from "Kang S, Lee S, Park S. iRGD Peptide as a Tumor-Penetrating Enhancer for Tumor-Targeted Drug Delivery. Polymers (Basel) 2020;12:1906." (24).

the tumors were measured. Four weeks later, the animals were intravenously injected with 10 nmol of iRGD-ZW800 in PBS. After 48 h, the skin on the tumor surface was removed, and the animals were anesthetized and placed on the operating table for imaging using FLI-10B. Tumors, muscles, and lung tissue were removed for imaging. After imaging, all tissues were fixed with 4% paraformaldehyde. Hematoxylin and eosin (H&E) sectioning showed that the spontaneous lung metastasis model was successfully established.

Statistical analysis

OriginPro 2016 and Graphpad10.1.2 were used to analyze the fluorescence intensity values. ImageJ (Wayne Rasband, National Institutes of Health, Bethesda, MD, USA, version 1.51j8, based on Java 1.8.0_112) was used to count the fluorescence intensity of mouse lung metastases, and Living Image Software (IVIS Spectrum Imaging Systems, Living Imaging 4.5.5) was used to count the fluorescence intensity

of mouse tumors and various organs.

Results

Schematic representation of iRGD-activated tumor targeting for tracer solid tumor delivery, as shown in *Figure 1*.

Rationale of iRGD-ZW800 design

We conducted the computational analysis using SMINA to calculate the binding energy of iRGD and iRGD-ZW800 with integrin αvβ3. Leveraging the high-resolution crystal structures of the receptor bound with small molecule inhibitors from the Protein Data Bank (PDB-ID 1L5G), we conducted molecular docking simulations. By substituting the co-crystalized ligand with iRGD and iRGD-ZW800, we examined their interactions within the binding pockets of the receptor. Our results revealed resemblances in both the binding modes and energies between iRGD (binding energy: –12.2 kcal/mol) and iRGD-ZW800 (binding
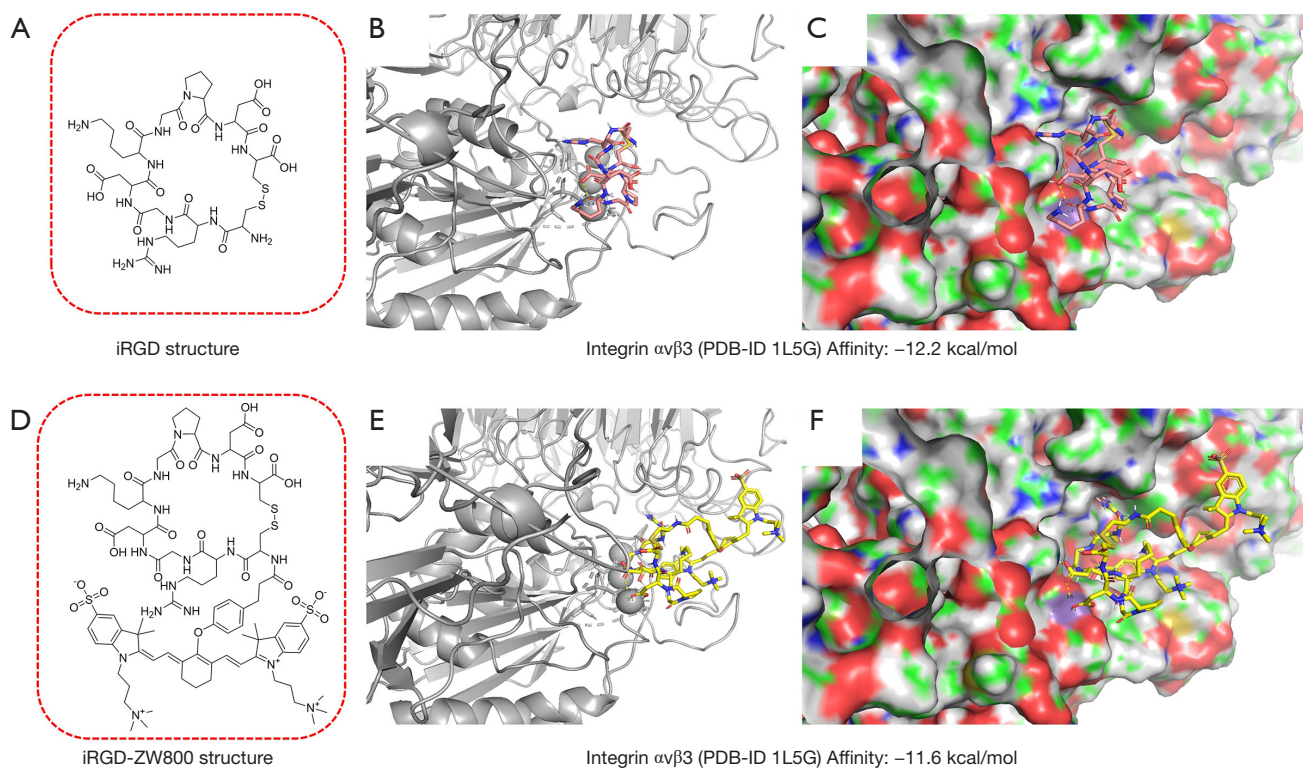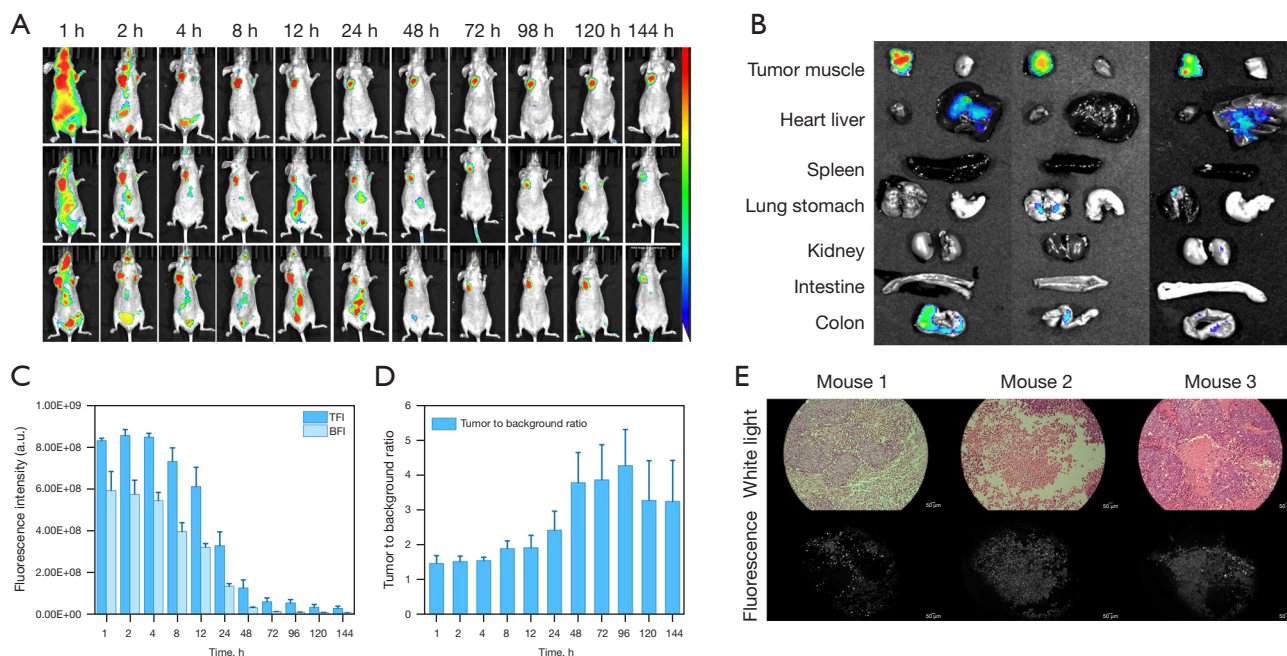
Figure 2 Molecular docking for integrin αvβ3 (PDB-ID 1L5G). (A) Structure of iRGD. (B,C) Integrin αvβ3 (PDB-ID 1L5G) and iRGD with a binding energy of –12.2 kcal/mol. (D) Structure of iRGD-ZW800. (E,F) Integrin αvβ3 (PDB-ID 1L5G) and iRGD-ZW800 with a binding energy of –11.6 kcal/mol.
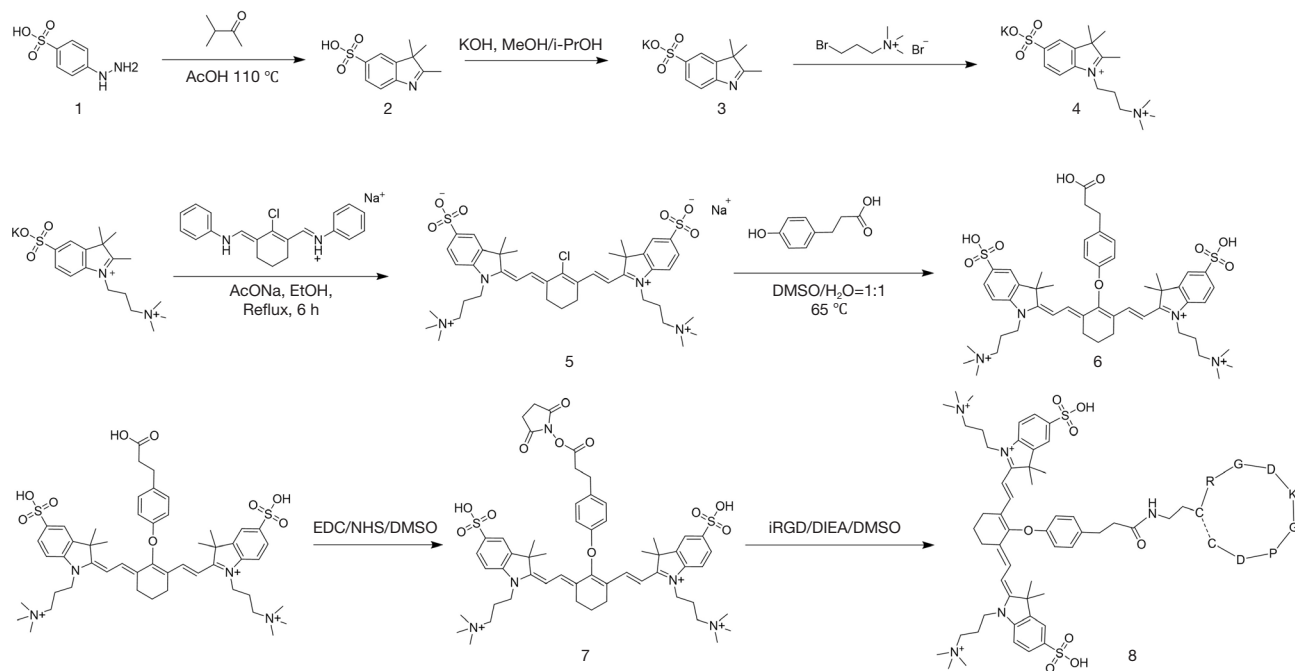
Figure 3 Synthesis scheme of iRGD-ZW800.

Figure 4 iRGD-ZW800 accumulates in αvβ3-overexpressed tumors. (A) Images of mice at various times after intravenous drug delivery. (B) 96 h after the delivery of 10 nmol of iRGD-ZW800, the mice bearing A549 were euthanized to determine the drug biodistribution. (C) Fluorescence intensity of the tumors and backgrounds at different time points. (D) The tumor-to-background ratios at different time points. (E) Each resected A549 tumor underwent microscopic fluorescent scanning. Staining method: place the slices in distilled water into a hematoxylin solution for several minutes, separate the slices in acid water and ammonia water for several seconds each, Rinse with running water for 1 hour and then place in distilled water for a while, dehydrate in 70% and 90% alcohol for 10 minutes each, stain in alcohol eosin staining solution for 2–3 minutes. Magnification is 10×.

energy: –11.6 kcal/mol) (*Figure 2*).

Structure and spectral properties of iRGD-ZW800

The synthesis of probe iRGD-ZW800 is shown in *Figure 3*. The structure of ZW800-1 was determined by proton nuclear magnetic resonance (^{1}H NMR) and carbon-13 nuclear magnetic resonance (^{13}C NMR) (Figures S1,S2). The purity of ZW800-1 was determined using HPLC and molecular weight of ZW800-1 was determined using LC-MS (Figures S3,S4). The molecular weight of iRGD-ZW800-1 was determined using LC-MS (Figure S5). The iRGD-ZW800 was further purified using prep-HPLC to ensure purity of >98% (Figure S6). Moreover, the probes iRGD-ZW800-1 and ZW800-1 showed a similar maximum absorption peak of about 770 nm, and a maximum emission wavelength of about 800 nm (Figure S7).

iRGD-ZW800 accumulates in αvβ3-overexpressed tumors

Mice bearing A549 subcutaneous tumors were evaluated to determine whether iRGD-ZW800 could specifically recognize αvβ3-expressing tumors. iRGD-ZW800 (n=3) was administered to the mice via a tail vein injection of 10 nmol, and then imaged periodically over 6 days. Strong background fluorescence was observed immediately after injection (*Figure 4A-4C*), and peak TBR was observed 96 h after injection at the 10 nmol dose level per animal (TBRmax =4.3±1.04) (*Figure 4D*).

We evaluated the biodistribution of iRGD-ZW800. Three mice bearing A549 subcutaneous tumors were injected with 10 nmol of iRGD-ZW800. After 96 hours, the mice were sacrificed, and the fluorescence intensity of multiple organs was obtained. The highest levels of fluorescence were observed in the A549 tumors, with low

Table 1 Fluorescence intensity ratio of different organs relative to muscles

ROTM	T/M	H/M	Li/M	Sp/M	L/M	Ki/M	St/M	In/M	C/M
Mouse 1	22.73	2.02	8.11	0.87	5.84	5.03	4.21	1.68	10.20
Mouse 2	19.22	1.63	4.60	1.03	7.17	5.93	5.18	1.85	7.41
Mouse 3	7.90	0.84	3.14	0.65	2.03	2.75	1.61	0.77	2.80
AVG	16.61	1.50	5.28	0.85	5.01	4.57	3.67	1.43	6.80
SD	7.75	0.60	2.55	0.19	2.67	1.64	1.85	0.58	3.74

ROTM, ratio of different organs to muscle; AVG, average; SD, standard deviation; T, tumor; M, muscle; H, heart; Li, liver; Sp, spleen; L, lung; Ki, kidney; St, stomach; In, intestine, C, colon.

fluorescence intensity observed in other organs (*Figure 4B*). The fluorescence intensity ratio of organs (T, tumor; H, heart; L, lung; S, spleen; Li, liver; K, kidney; In, intestine; C, colon) to muscle was showed in Figure S8. The fluorescence intensity ratios of each organ and muscle are listed in *Table 1*. The co-culturing of fluorescent molecule iRGD-ZW800 with cells demonstrates excellent biocompatibility, allowing for their interaction within cellular systems (Figure S9). The fluorescent molecules exhibit high compatibility with cellular environments, enabling efficient uptake and intracellular localization without inducing adverse effects. The fluorescence intensity of the tumor to muscle ratio *ex vivo* was significantly higher than that *in vivo*. This result is caused by the fluorescence of the skin. Finally, we determined through the fluorescence intensity of the H&E slices that iRGD-ZW800 can achieve specific targeted imaging at the tumor cell level using fluorescence microscopy (*Figure 4E*).

Orthotopic pulmonary LLC tumor imaging and boundary analysis

Given the high tumor fluorescence and low signal of the benign lungs, we believed that iRGD-ZW800 could accumulate within orthotopic LLC pulmonary xenografts. The detailed experimental procedure is shown in (*Figure 5A*). The mice with established pulmonary xenografts were injected via the tail vein with 10 nmol of iRGD-ZW800. The control group mice were injected with ICG (100 nmol). At the study endpoint (24 h), the chest of each mouse was opened, and the lungs and tumors were exposed and imaged using the FLI-10B imaging system. Compared with the ICG control group, the iRGD-ZW800 group showed strong fluorescence in the tumor area (*Figure 5B*). Calculated using imageJ software, the ratio

of tumor to lung fluorescence intensity was 2.2 (standard deviation: 0.18) (*Figure 5C*).

We used a straight line passing through the lung parenchyma and the lung tumor area, and ImageJ to measure the fluorescence intensity changes along the straight line. We counted the distribution of fluorescence intensity in the tumor boundary region over a straight line distance between iRGD-ZW800 and ICG, and the results showed that the former had an s-curve distribution in the boundary distribution, and the fluorescence intensity at the boundary decreased faster than that of ICG (368/cm *vs.* 192/cm), confirming that iRGD-ZW800 differentiated the tumor boundary more clearly (*Figure 5D*).

Detection of metastatic nodules in vivo

Further insights into the sensitivity of iRGD-ZW800 were gained through the detection of metastatic nodules in mice bearing 4T1 tumors, which are known to develop into metastatic lesions in the lungs. Four hours post-intravenous injection, fluorescence signals from iRGD-ZW800 were observed in the lungs of the mice upon dissection. When compared to the imaging results obtained from ICG, iRGD-ZW800 demonstrated a superior ability to detect more nodules (*Figure 6*).

In the spontaneous breast cancer lung metastasis model, the skin overlying the subcutaneous tumor was removed 48 h after the tail vein injection of 10 nmol of iRGD-ZW800. The findings indicated that iRGD-ZW800 not only precisely localized the 4T1 subcutaneous tumors but also made the metastatic nodules in the lungs clearly visible through isolated trachea assays (*Figure 7A,7B*). In the first mouse, a series of metastatic lung nodules were detected, with a fluorescence intensity more than 2.3 times higher than that of the surrounding normal lung tissue.
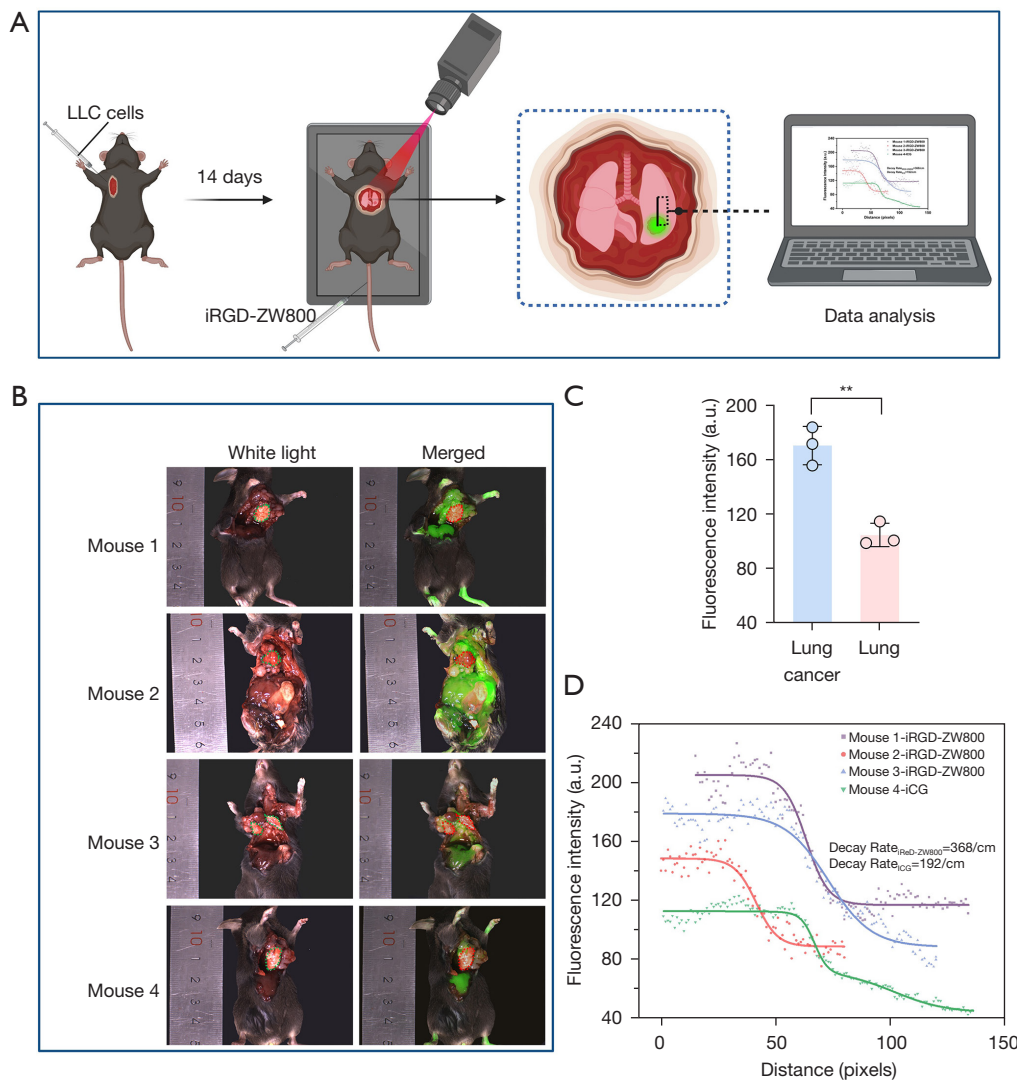
Figure 5 Orthotopic pulmonary LLC tumor imaging and boundary analysis. (A) Flowchart of experimental procedures. (B) Orthotopic pulmonary LLC tumor imaging with FLI-10B. (C) Comparison of fluorescence intensity between LLC cancer and normal lung tissue (P<0.01). (D) Comparison of the boundaries between iRGD-ZW800 and ICG in distinguishing lung cancer. **, P<0.01. a.u., arbitrary unit; LLC, Lewis lung carcinoma; ICG, indocyanine green.

Remarkably, in the third mouse, the fluorescence intensity of the metastatic nodules was 4.2 times higher than that of the normal lung tissue, surpassing the tumor-to-muscle fluorescence intensity ratio (*Figure 7C*). This observation was further confirmed by the H&E staining, which verified the presence of metastases in the lungs of all three mice to varying degrees. Our imaging results validate the potential clinical application of iRGD-ZW800 in detecting lung metastases with high expressions of αvβ3. This offers physicians a more effective tool for identifying metastatic lung nodules (*Figure 7D*).

Discussion

With the popularity of low-dose spiral CT screening, lung nodules are increasingly being detected and staged earlier (25-27). The standard treatment for early stage NSCLC is radical lobectomy (28). In clinical practice, wedge resection has been shown to preserve more lung function and provide a significantly better quality of life for patients than lobectomy (29). However, while wedge resection has these advantages, the incidence of postoperative recurrence, including incisional margin recurrence, is also gradually
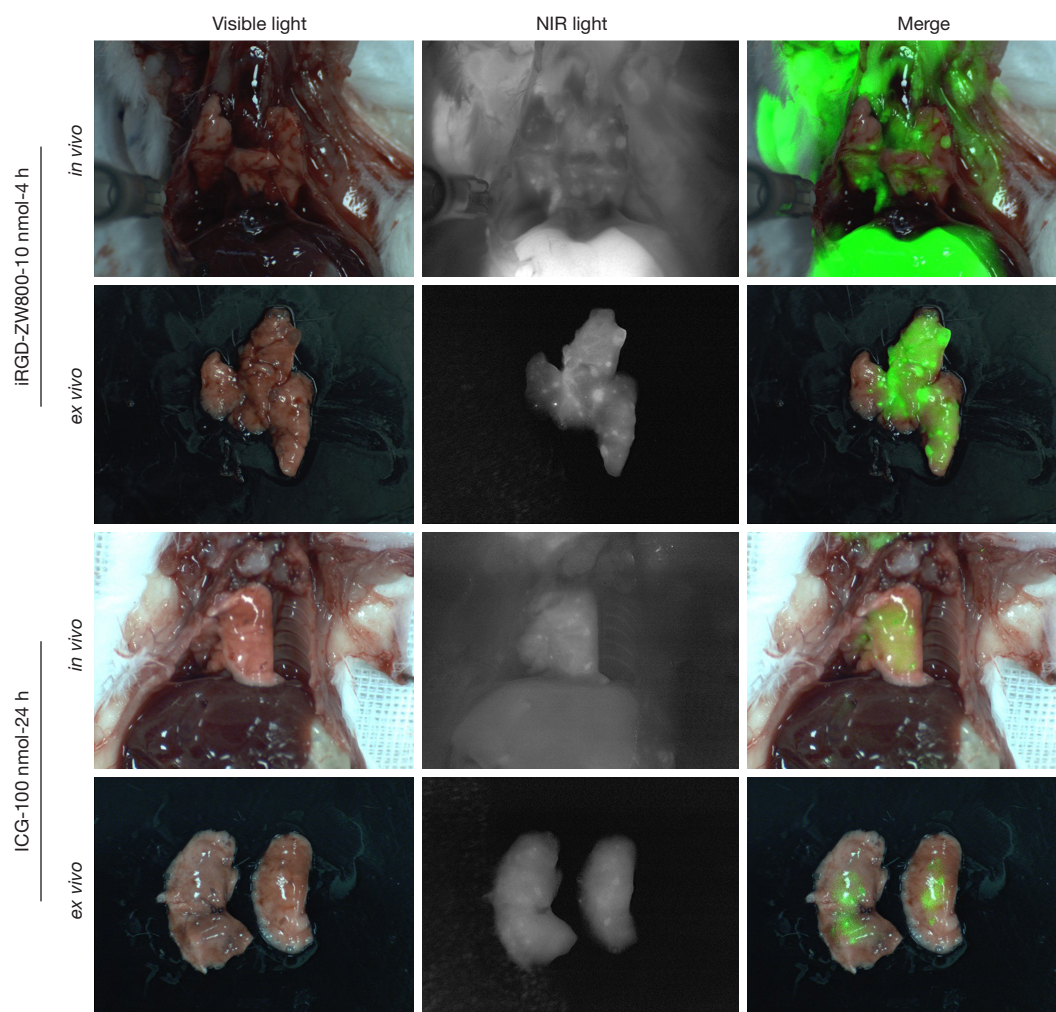
Figure 6 Comparison of pulmonary nodule detection between iRGD-ZW800 (10 nmol, 4 h) and ICG (100 nmol, 24 h). NIR, near-infrared; ICG, indocyanine green.

increasing (30-33). The question of how to accurately locate lung nodules to effectively prevent damage to normal lung tissue is an important clinical problem that needs to be solved. The methods currently used for lung nodule localization include CT-guided percutaneous localization markers (34,35), bronchoscopic localization markers (36), intraoperative ultrasound (37), artificial intelligence (38) assisted identification, and intraoperative molecular imaging (39). NIFR has several unique advantages over other techniques; for example, it has no radiation, is non-invasive, has the ability to penetrate organs and tissues to improve imaging, and has the ability to localize nodules in real-time intraoperatively and intuitively (40). Thus, it will likely become the future trend of intraoperative localization.

Based on the high expression of αvβ3 on the surface

of tumor cells, the iRGD peptide has been extensively investigated for tumor imaging using various imaging modalities (41-45). Phase I clinical trials are currently being conducted to evaluate the efficacy and safety of cRGD-ZW800-1 in patients with colorectal cancer (46). In this study, we took advantage of iRGD's high affinity for αvβ3 overexpression in lung cancer and its ability to target the NPR1 receptor to penetrate the cell membrane and deliver a fluorescent tracer into tumor cells, which not only achieves deep tumor-permeable imaging, but also results in a slower tumor clearance rate, and extends the tumor imaging window. Since the mouse spontaneous lung tumor model has similar morphological, histological and molecular characteristics to human lung cancer (18), we further investigated the effect of iRGD-ZW800 on lung
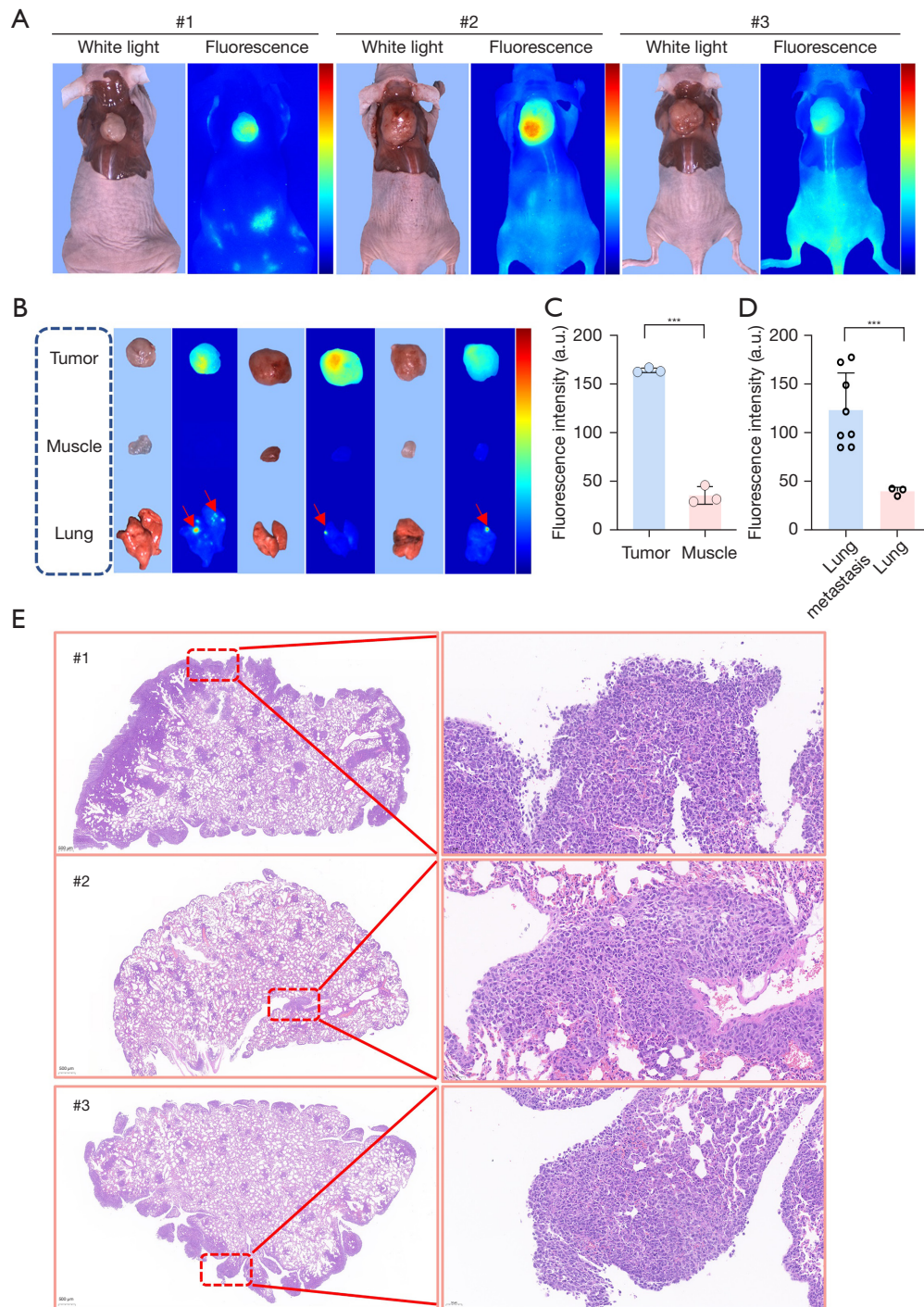
Figure 7 Detection of spontaneous lung metastases with iRGD-ZW800 at 48 h. (A) Imaging of 4T1 subcutaneous tumors in nude mice (n=3). (B) White light and fluorescence image of *ex vivo* tumor, muscle, and lung with metastatic nodules. Arrows were used to indicate tumor location. (C) Analysis of fluorescence intensity of tumor and muscle. (D) Analysis of fluorescence intensity of metastatic lung nodules and normal lung tissue. (E) Histological examination of nodules in three regions of interest of a metastatic lung. Scale bar: left, 500 µm; right, 50 µm. Staining method: place the slices in distilled water into a hematoxylin solution for several minutes, separate the slices in acid water and ammonia water for several seconds each, rinse with running water for 1 hour and then place in distilled water for a while, dehydrate in 70% and 90% alcohol for 10 minutes each, stain in alcohol eosin staining solution for 2–3 minutes. a.u., arbitrary unit.

tumor imaging in C57BL/6J mice. The imaging results showed that the tumor background ratios of iRGD-ZW800 imaging were all greater than 1.5, enabling the lung tumors to be visualized.

Many triple negative breast cancer patients also have high rates of brain and lung metastases at advanced stages (47). The molecular targeting of lung metastases is challenging because metastatic foci are smaller, more dispersed, and less vascularized than primary tumors, making it more difficult for molecular probes to reach these lesions (48,49). Notably, in terms of its specificity and sensitivity, iRGD-ZW800 demonstrated an excellent ability to detect millimeter-sized small tumor metastases (*Figure* 7), with the histopathological assessment of H&E staining further confirming that the hyperfluorescent areas were tumor areas. This represents a significant improvement in fluorescence imaging.

The most clinically used fluorescent tracer, ICG, is currently used in NIRF to navigate tumor surgery. However, its use in NIRF navigation in tumor surgery is greatly restricted by its poor specificity (including its accumulation in inflammatory areas), and an inability to determine the optimal dose and timing of the procedure. Researchers have sought to find a targeted molecular visualizer that specifically binds to and identifies lung adenocarcinoma. Epidermal growth factor receptor (EGFR) (50), interleukins (51), folate receptor (52), and integrin $\alpha v\beta 3$ (53) are highly expressed in lung cancer, and have been shown to be promising therapeutic targets for lung cancer. cRGD-ZW800-1, which was developed by de Valk and other investigators, was evaluated for the first time in humans in colon cancer, and the results confirmed that cRGD-ZW800-1 was able to fluorescently image colon cancers in both open and minimally invasive procedures. Given the widespread overexpression of integrin $\alpha v\beta 3$ in lung cancer, cRGD-ZW800-1 may need to be developed further before it can be widely used in lung cancer surgery. cRGD-ZW800-1 was developed by Low and other investigators as a near-infrared fluorescent tracer, OTL-38, which is now being successfully used in lung and ovarian cancers, but because OTL-38 has the same affinity for both the α and β receptors, and the folate receptor-β is also highly expressed in tissues containing a large number of macrophages, there is still a 32.7% false-positive rate (54). Therefore, we chose iRGD as the targeting moiety in the present study. iRGD-conjugated drugs specifically bind to integrin $\alpha v\beta 3$, which is overexpressed in various tumors, and cleave to NRP-1, thus triggering NRP-1-dependent endocytosis, thereby enhancing tumor penetration (24).

Thus, such drugs are suitable for localizing lesions deep in the lung parenchyma.

Limitations

In this study, we did not directly compare cRGD-ZW800 and iRGD-ZW800 in terms of the depth of tumor penetration; however, we intend to explore this in future experiments. Undoubtedly, the increase in tracer penetration depth will assist doctors to locate deeper hidden tumors, which will improve the high fluorescence background caused by the free diffusion of non-targeted tracers, and also alter the current inability of targeted tracers to penetrate into tumors, which has already been validated in oncology treatments.

Conclusions

In conclusion, a facile method for the synthesis of iRGD-ZW800 tracer was developed. The molecule has absorption and emission wavelengths in the near-infrared region and has good water solubility. The purity of the prepared iRGD-ZW800 was over 98%. The fluorescent tracer can specifically target tumor cells for imaging. Small animal imaging showed that iRGD-ZW800 effectively entered the tumor spheroid to achieve the imaging of single cells in the tumor tissue and had a long tumor imaging window. Finally, iRGD-ZW800 was shown to be promising in the real-time imaging of primary lung cancer and lung metastases in various lung tumor models.

Acknowledgments

Footnote

Reporting Checklist: The authors have completed the ARRIVE reporting checklist. Available at https://tlcr.

amegroups.com/article/view/10.21037/tlcr-24-589/rc

References

1. Leiter A, Veluswamy RR, Wisnivesky JP. The global burden of lung cancer: current status and future trends. Nat Rev Clin Oncol 2023;20:624-39.

2. Aliperti LA, Predina JD, Vachani A, et al. Local and systemic recurrence is the Achilles heel of cancer surgery. Ann Surg Oncol 2011;18:603-7.

3. Aokage K, Yoshida J, Hishida T, et al. Limited resection for early-stage non-small cell lung cancer as function-preserving radical surgery: a review. Jpn J Clin Oncol 2017;47:7-11.

4. Battafarano RJ, Meyers BF, Guthrie TJ, et al. Surgical resection of multifocal non-small cell lung cancer is associated with prolonged survival. Ann Thorac Surg 2002;74:988-93; discussion 993-4.

5. Tierney JF, Chivukula SV, Wang X, et al. Resection of primary tumor may prolong survival in metastatic gastroenteropancreatic neuroendocrine tumors. Surgery 2019;165:644-51.

6. Lee J, Wang N, Turk S, et al. Discriminating pseudoprogression and true progression in diffuse infiltrating glioma using multi-parametric MRI data through deep learning. Sci Rep 2020;10:20331.

7. de Koning HJ, van der Aalst CM, de Jong PA, et al. Reduced Lung-Cancer Mortality with Volume CT Screening in a Randomized Trial. N Engl J Med 2020;382:503-13.

8. Li L, Wu Y, Wang Z, et al. SPECT/CT Imaging of the Novel HER2-Targeted Peptide Probe (99m)Tc-HYNIC-H6F in Breast Cancer Mouse Models. J Nucl Med 2017;58:821-6.

9. McDonald ES, Clark AS, Tchou J, et al. Clinical Diagnosis and Management of Breast Cancer. J Nucl Med 2016;57 Suppl 1:9S-16S.

10. Pogue BW, Rosenthal EL. Review of successful pathways for regulatory approvals in open-field fluorescence-guided surgery. J Biomed Opt 2021;26:030901.

11. Jiang JX, Keating JJ, Jesus EM, et al. Optimization of the enhanced permeability and retention effect for near-infrared imaging of solid tumors with indocyanine green. Am J Nucl Med Mol Imaging 2015;5:390-400.

12. Li Y, You Q, Wang Z, et al. A study on setting standards for near-infrared fluorescence-image guided surgery (NIRFGS) time lapse monitoring based on preoperative liver function assessment. Ann Transl Med 2022;10:96.

13. Zhou D, Thinn AMM, Zhao Y, et al. Structure of an extended β(3) integrin. Blood 2018;132:962-72.

14. Desgrosellier JS, Cheresh DA. Integrins in cancer: biological implications and therapeutic opportunities. Nat Rev Cancer 2010;10:9-22.

15. Choi HS, Gibbs SL, Lee JH, et al. Targeted zwitterionic near-infrared fluorophores for improved optical imaging. Nat Biotechnol 2013;31:148-53.

16. Alsibai W, Hahnenkamp A, Eisenblätter M, et al. Fluorescent non-peptidic RGD mimetics with high selectivity for αVβ3 vs αIIbβ3 integrin receptor: novel probes for in vivo optical imaging. J Med Chem 2014;57:9971-82.

17. Attieh Y, Clark AG, Grass C, et al. Cancer-associated fibroblasts lead tumor invasion through integrin-β3-dependent fibronectin assembly. J Cell Biol 2017;216:3509-20.

18. de Valk KS, Deken MM, Handgraaf HJM, et al. First-in-Human Assessment of cRGD-ZW800-1, a Zwitterionic, Integrin-Targeted, Near-Infrared Fluorescent Peptide in Colon Carcinoma. Clin Cancer Res 2020;26:3990-8.

19. Qin W, Chandra J, Abourehab MAS, et al. New opportunities for RGD-engineered metal nanoparticles in cancer. Mol Cancer 2023;22:87.

20. Llaguno-Munive M, Villalba-Abascal W, Avilés-Salas A, et al. Near-Infrared Fluorescence Imaging in Preclinical Models of Glioblastoma. J Imaging 2023;9:212.

21. Ruoslahti E. Tumor penetrating peptides for improved drug delivery. Adv Drug Deliv Rev 2017;110-111:3-12.

22. Simón-Gracia L, Hunt H, Teesalu T. Peritoneal Carcinomatosis Targeting with Tumor Homing Peptides. Molecules 2018;23:1190.

23. Hyun H, Bordo MW, Nasr K, et al. cGMP-Compatible preparative scale synthesis of near-infrared fluorophores. Contrast Media Mol Imaging 2012;7:516-24.

24. Kang S, Lee S, Park S. iRGD Peptide as a Tumor-Penetrating Enhancer for Tumor-Targeted Drug Delivery. Polymers (Basel) 2020;12:1906.

25. Li X, Zhang W, Yu Y, et al. CT features and quantitative analysis of subsolid nodule lung adenocarcinoma for pathological classification prediction. BMC Cancer 2020;20:60.

26. Hiramatsu M, Inagaki T, Inagaki T, et al. Pulmonary ground-glass opacity (GGO) lesions-large size and a history of lung cancer are risk factors for growth. J Thorac Oncol 2008;3:1245-50.

27. Koike T, Koike T, Yoshiya K, et al. Risk factor analysis of locoregional recurrence after sublobar resection in patients with clinical stage IA non-small cell lung cancer. J Thorac Cardiovasc Surg 2013;146:372-8.

28. Maniwa T, Okami J, Miyoshi T, et al. Lymph node dissection in small peripheral lung cancer: Supplemental analysis of JCOG0802/WJOG4607L. J Thorac Cardiovasc Surg 2023;S0022-5223(23)01099-1.

29. Jiang S, Wang B, Zhang M, et al. Quality of life after lung cancer surgery: sublobar resection versus lobectomy. BMC Surg 2023;23:353.

30. Nelson DB, Tayob N, Mitchell KG, et al. Surgical margins and risk of local recurrence after wedge resection of colorectal pulmonary metastases. J Thorac Cardiovasc Surg 2019;157:1648-55.

31. Masai K, Sakurai H, Sukeda A, et al. Prognostic Impact of Margin Distance and Tumor Spread Through Air Spaces in Limited Resection for Primary Lung Cancer. J Thorac Oncol 2017;12:1788-97.

32. Mastrobuoni S, de Kerchove L, Navarra E, et al. Long-term experience with valve-sparing reimplantation technique for the treatment of aortic aneurysm and aortic regurgitation. J Thorac Cardiovasc Surg 2019;158:14-23.

33. Mohiuddin K, Haneuse S, Sofer T, et al. Relationship between margin distance and local recurrence among patients undergoing wedge resection for small (≤2 cm) non-small cell lung cancer. J Thorac Cardiovasc Surg 2014;147:1169-75; discussion 1175-7.

34. Park CH, Han K, Hur J, et al. Comparative Effectiveness and Safety of Preoperative Lung Localization for Pulmonary Nodules: A Systematic Review and Meta-analysis. Chest 2017;151:316-28.

35. Jiang T, Lin M, Zhao M, et al. Preoperative Computed Tomography-Guided Localization for Pulmonary Nodules with Glue and Dye. Thorac Cardiovasc Surg 2020;68:525-32.

36. Okumura T, Kondo H, Suzuki K, et al. Fluoroscopy-assisted thoracoscopic surgery after computed tomography-guided bronchoscopic barium marking. Ann Thorac Surg 2001;71:439-42.

37. Ost DE, Ernst A, Lei X, et al. Diagnostic Yield and Complications of Bronchoscopy for Peripheral Lung Lesions. Results of the AQuIRE Registry. Am J Respir Crit Care Med 2016;193:68-77.

38. Zhang L, Wang L, Kadeer X, et al. Accuracy of a 3-Dimensionally Printed Navigational Template for Localizing Small Pulmonary Nodules: A Noninferiority Randomized Clinical Trial. JAMA Surg 2019;154:295-303.

39. Sarkaria IS, Martin LW, Rice DC, et al. Pafolacianine for intraoperative molecular imaging of cancer in the

lung: The ELUCIDATE trial. J Thorac Cardiovasc Surg 2023;166:e468-78.

40. Mieog JSD, Achterberg FB, Zlitni A, et al. Fundamentals and developments in fluorescence-guided cancer surgery. Nat Rev Clin Oncol 2022;19:9-22.

41. Bohn P, Modzelewski R, Rouvet J, et al. Biodistribution and imaging of [99mTc]-HYNIC-RGD in MDA-MB-231 and NTERA-2 cancer cell xenografts. Nucl Med Commun 2013;34:709-17.

42. Zuo HD, Yao WW, Chen TW, et al. The effect of superparamagnetic iron oxide with iRGD peptide on the labeling of pancreatic cancer cells in vitro: a preliminary study. Biomed Res Int 2014;2014:852352.

43. Li Y, Feng X, Lu Z, et al. Enhanced photocatalytic H(2)-production activity of C-dots modified g-C(3)N(4)/TiO(2) nanosheets composites. J Colloid Interface Sci 2018;513:866-76.

44. Yu B, Su H, Zhao L, et al. (99m)Tc-labeled iRGD for single-positron emission computed tomography imaging of triple-negative breast cancer. Front Bioeng Biotechnol 2022;10:1001899.

45. Cho HJ, Lee SJ, Park SJ, et al. Activatable iRGD-based peptide monolith: Targeting, internalization, and fluorescence activation for precise tumor imaging. J Control Release 2016;237:177-84.

46. Meuwissen R, Berns A. Mouse models for human lung cancer. Genes Dev 2005;19:643-64.

47. Carey L, Winer E, Viale G, et al. Triple-negative breast cancer: disease entity or title of convenience? Nat Rev Clin Oncol 2010;7:683-92.

48. Cao H, Dan Z, He X, et al. Liposomes Coated with Isolated Macrophage Membrane Can Target Lung Metastasis of Breast Cancer. ACS Nano 2016;10:7738-48.

49. Duan X, Chan C, Guo N, et al. Photodynamic Therapy Mediated by Nontoxic Core-Shell Nanoparticles Synergizes with Immune Checkpoint Blockade To Elicit Antitumor Immunity and Antimetastatic Effect on Breast Cancer. J Am Chem Soc 2016;138:16686-95.

50. Lee HJ, Seo AN, Kim EJ, et al. Prognostic and predictive values of EGFR overexpression and EGFR copy number alteration in HER2-positive breast cancer. Br J Cancer 2015;112:103-11.

51. Haura EB, Livingston S, Coppola D. Autocrine interleukin-6/interleukin-6 receptor stimulation in non-small-cell lung cancer. Clin Lung Cancer 2006;7:273-5.

52. Mahalingam SM, Kularatne SA, Myers CH, et al. Evaluation of Novel Tumor-Targeted Near-Infrared Probe for Fluorescence-Guided Surgery of Cancer. J Med Chem 2018;61:9637-46.

53. Gu Y, Dong B, He X, et al. The challenges and opportunities of αvβ3-based therapeutics in cancer: From bench to clinical trials. Pharmacol Res 2023;189:106694.

54. Tanyi JL, Randall LM, Chambers SK, et al. A Phase III Study of Pafolacianine Injection (OTL38) for Intraoperative Imaging of Folate Receptor-Positive Ovarian Cancer (Study 006). J Clin Oncol 2023;41:276-84.